

Directing CO₂ electroreduction pathways for selective C₂ product formation using single-site doped copper catalysts

Zhengyuan Li^{1,9}, Peng Wang^{2,9}, Xiang Lyu³, Vamsi Krishna Reddy Kondapalli⁴, Shuting Xiang^{5,6}, Juan D. Jimenez⁶, Lu Ma⁷, Takeshi Ito¹, Tianyu Zhang¹, Jithu Raj¹, Yanbo Fang⁴, Yaocai Bai³, Jianlin Li³, Alexey Serov³, Vesselin Shanov^{1,4}, Anatoly I. Frenkel^{5,6}, Sanjaya D. Senanayake⁶, Shize Yang^{8*}, Thomas P. Senftle^{2*} and Jingjie Wu^{1*}

¹ Department of Chemical and Environmental Engineering, University of Cincinnati, Cincinnati, OH 45221, USA

² Department of Chemical and Biomolecular Engineering, Rice University, Houston, TX 77005, USA

³ Electrification and Energy Infrastructures Division, Oak Ridge National Laboratory, Oak Ridge, TN 37831, USA

⁴ Department of Mechanical and Materials Engineering, University of Cincinnati, Cincinnati, OH 45221, USA

⁵ Department of Materials Science and Chemical Engineering, Stony Brook University, Stony Brook, NY 11794, USA

⁶ Chemistry Division, Brookhaven National Laboratory, Upton, NY 11973, USA

⁷ National Synchrotron Light Source II, Brookhaven National Laboratory, Upton, NY 11971, USA

⁸ Eyring Materials Center, Arizona State University, Tempe, AZ 85287, USA

⁹ These authors contributed equally: Zhengyuan Li, Peng Wang.

*email: shize.yang@asu.edu; tsenftle@rice.edu; jingjie.wu@uc.edu

Abstract

Manipulating the selectivity-determining step in post-C–C coupling is crucial for enhancing C₂ product specificity during electrocatalytic CO₂ reduction, complementing efforts to boost rate-determining step kinetics. Here we highlight the role of single-site noble metal dopants on Cu surfaces in influencing C–O bond dissociation in an oxygen-bound selectivity-determining intermediate, steering post-C–C coupling toward ethylene versus ethanol. Integrating theoretical and experimental analyses, we demonstrate that the oxygen binding strength of the Cu surface controls the favorability of C–O bond scission, thus tuning the selectivity ratio of ethylene-to-ethanol. The Rh-doped Cu catalyst with optimal oxygen binding energy achieves a Faradaic efficiency toward ethylene of 61.2% and an ethylene-to-ethanol Faradaic efficiency ratio of 4.51 at –0.66 V versus RHE (reversible hydrogen electrode). Integrating control of both rate-determining and selectivity-determining steps further raises ethylene Faradaic efficiency to 68.8% at 1.47 A cm^{–2} in a tandem electrode. Our insights guide the rational design of Cu-based catalysts for selective CO₂ electroreduction to a single C₂ product.

Introduction

Copper-based catalysts drive the electrochemical CO₂ reduction reaction (CO₂RR) to produce fuels and chemicals containing multi-carbon centers (C₂₊)^{1,2}. However, Cu catalysts suffer from a wide distribution of products, making the electrocatalytic CO₂-to-C₂₊ conversion far from a practical application². So far, tremendous efforts have been devoted to improving the selectivity of overall C₂₊ products through enhancing the binding energy of adsorbed CO (*CO) or increasing local CO concentration^{2,3}. These two interplayed parameters govern the kinetics of C–C coupling, which is regarded as the rate-determining step (RDS) for C₂₊ products formation^{2,3}. Experimental observations suggest the pathways toward ethylene (C₂H₄) and ethanol (C₂H₅OH), the two major C₂ products in CO₂RR, share several common intermediates until the bifurcation step at the post-C–C coupling stage^{4,5}. The relative stability of a selectivity-determining intermediate (SDI) determines the bifurcation leading to C₂H₄ vs. C₂H₅OH (refs.^{6–10}). The control of bifurcation at the post-C–C coupling stage, which is generally neglected in previous design attempts, is equally crucial as promoting C–C coupling kinetics in determining the selectivity toward a specific C₂ product.

Compared with the progress made in understanding the mechanisms of C–C coupling steps, identifying the SDI remains elusive, partially owing to the incapability of state-of-the-art operando technologies to probe the key C₂ intermediate directly. Density functional theory (DFT) studies dominate the research on the late stages of CO₂RR, which proposed variable SDIs with tautomeric forms^{6–9}. The SDI configurations can be classified based on the atom(s) coordinated on the Cu surface: carbon-bound (e.g., Cu–C–OH) or oxygen-bound (e.g., Cu–O–C) structures^{6–9}. Previous studies developed various catalysts to enhance C₂H₅OH generation over C₂H₄ and applied different SDI structures to rationalize their selectivity-determining steps (SDSs)^{11–17}. However, the key SDI branching C₂ alcohol and hydrocarbon has not been validated by a generalized catalyst design strategy.

Regulating the C–O bond strength of the SDI is critical to direct the pathways to hydrocarbons

vs. oxygenates¹⁸⁻²². In particular, the cleavage vs. preservation of the C–O bond in the oxygen-bound SDI (e.g., *CH₂CHO) determines the selectivity toward C₂H₄ vs. C₂H₅OH production^{9,10}. The hydrogenation of *CH₂CHO leads to either the formation of acetaldehyde (*CH₃CHO, the precursor to C₂H₅OH) or the desorption of C₂H₄ with adsorbed oxygen (*O) remaining on the catalyst surface⁹. The relative stability of *O species after C–O bond cleavage is an adequate descriptor to evaluate the potential bifurcation to C₂H₄ vs. C₂H₅OH formation¹⁰. According to the linear scaling relation, the effect of oxygen binding strength translates to the adsorption configurations and energetics of oxygen-bound intermediates and resultant product selectivity^{10,21-26}.

Herein we report a generalized concept of tuning oxygen affinity²⁷ to direct post-C–C coupling selectivity toward C₂H₄ or C₂H₅OH via the stabilization and activation of *O and *CH₂CHO intermediates on single-site noble metal doped Cu catalysts (M-Cu, M = Rh, Ir, Ru, Pd, Ag, and Au). The oxygen binding strength on M-Cu surface dictates the cleavage and preservation of the C–O bond in the *CH₂CHO intermediate. Specifically, Rh-Cu could efficiently shift the product distribution toward C₂H₄ at the expense of C₂H₅OH, compared to the bare Cu. DFT calculations reveal that the Rh dopant with stronger oxygen affinity than Cu stabilizes *CH₂CHO adsorption and elongates C–O bond length (thus weakening the bond strength) while still warranting energy-efficient *O hydrogenation to H₂O after C–O bond scission. In contrast, dopants with weaker oxygen affinity than Cu, such as Au, promote C₂H₅OH formation by preserving the C–O bond. Our studies offer a universal reaction descriptor to rationalize catalyst design for selective CO₂RR toward a single C₂ product.

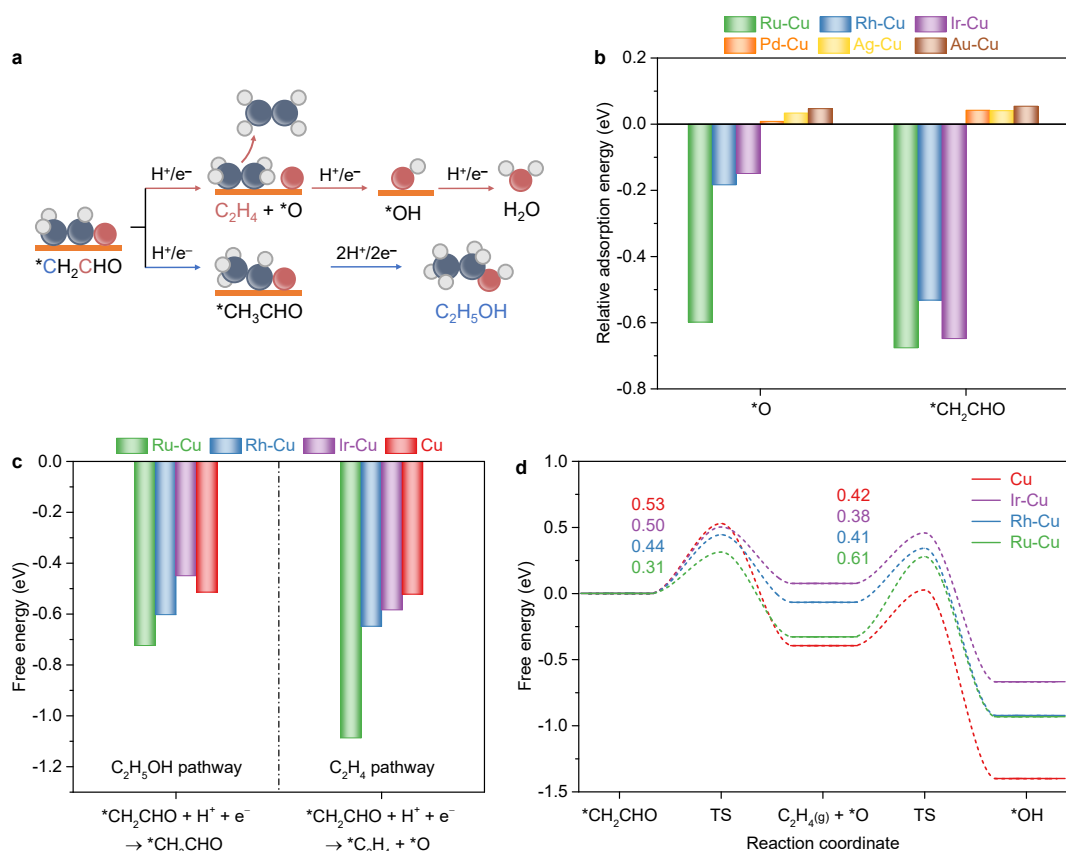


Fig. 1 DFT calculations. **a**, Schematic illustration of branching pathways to C_2H_4 and C_2H_5OH from $*CH_2CHO$ intermediate as the SDI. The black, red, and white balls represent C, O, and H atoms, respectively. **b**, Adsorption energies of $*O$ and $*CH_2CHO$ intermediates on M-Cu catalysts relative to pristine Cu. **c**, Reaction free energy for first hydrogenation steps of $*CH_2CHO$ intermediate to C_2H_5OH and C_2H_4 over pristine Cu and oxophilic M-Cu catalysts. **d**, Free energy diagrams under -0.65 V bias potential for hydrogenation of $*CH_2CHO$ intermediate to C_2H_4 and $*OH$ on pristine Cu and oxophilic M-Cu catalysts. The numbers are kinetic barrier values in eV.

Results

Catalyst design principles. The SDI of $*CH_2CHO$ species initially proposed by Koper and co-workers originates from four proton-coupled electron transfer steps of the $*COCO$ H intermediate in sequence following the C–C coupling⁹. The C_2H_4 pathway proceeds via C–O bond scission, releasing C_2H_4 and leaving an adsorbed $*O$ (Fig. 1a). The $*O$ adsorbate is protonated to $*OH$ and then to H_2O . Alternatively, the hydrogenation of α -carbon in $*CH_2CHO$ leads to $*CH_3CHO$ and consequently to C_2H_5OH , where C–O bond is preserved (Fig. 1a). We postulate that doping single-

site metals with distinct oxygen binding abilities than Cu can modulate the C–O bond strength in the SDI. A library of single-site noble metal dopants, including Rh, Ir, Ru, Pd, Ag, and Au, is computationally screened, because they can dope into Cu matrix in a thermodynamically favorable way²⁸.

We first investigated the relative adsorption stability of *O, *CH₂CHO, and other related intermediates along the post-C–C coupling reaction pathways (Fig 1b and Supplementary Fig. 1). Pd, Ag, and Au dopants with weaker oxygen binding abilities than Cu induce slight impact on the adsorption energies or configurations of oxygen-bound intermediates. The *O adsorbate prefers sitting on a hollow site comprising four Cu atoms (Cu₄ sites) over that comprising one dopant and three Cu atoms (i.e., Cu₃Ag, Cu₃Au and Cu₃Pd sites) at the low doping concentration (Supplementary Fig. 2). The weaker oxygen binding is also evidenced by the downshift of *d*-band center after Ag doping (from –2.09 eV to –2.35 eV) (Supplementary Fig. 3). Oppositely, in the case of dopants with stronger oxygen binding abilities than Cu, Cu₃M (M = Rh, Ir and Ru) sites directly participates in the stabilization of *O species (Supplementary Fig. 2c). The *d*-band center of Cu₃Rh site on Rh-Cu is shifted up to –1.97 eV, which corroborates the stronger adsorption features (Supplementary Fig. 3). As reflected by the adsorption energy of *O atom²¹, the oxygen affinity of M-Cu catalysts decreases in the order: Ru-Cu > Rh-Cu > Ir-Cu > Cu > Pd-Cu > Ag-Cu > Au-Cu.

The stronger interaction between *CH₂CHO and catalyst surface with enhanced oxygen affinity gives rise to the elongation of the C–O bond length in *CH₂CHO intermediate, and thus a weakened C–O bond strength¹⁰. The C–O bond lengths for oxophilic M-Cu (M = Rh, Ir, and Ru) surfaces are 1.355-1.367 Å, significantly longer than those for pristine Cu (1.320 Å) and oxophobic M-Cu (M = Pd, Ag, and Au) surfaces (1.319-1.320 Å) (Supplementary Table 1). Those oxophilic surfaces are hypothesized to efficiently direct the bifurcation to C₂H₄ by promoting C–O bond scission.

We then focused on theoretical analyses of elementary steps of the *CH₂CHO hydrogenation

on pristine Cu and oxophilic M-Cu surfaces. The C–O bond of *CH₂CHO is cleaved to produce C₂H₄ more thermodynamically feasible than being preserved to form *CH₃CHO and C₂H₅OH on oxophilic M-Cu surfaces, especially on the Ru-Cu (Fig. 1c). Reaction free energies of the following *O protonation step in C₂H₄ pathway are also largely influenced owing to improved oxygen affinities (Supplementary Fig. 4). We further calculated the kinetic barriers for C₂H₄ pathway as shown in Fig. 1d and Supplementary Fig. 5. The activation energy barrier for the C–O bond scission decreases as surface oxygen affinity increases. However, the *O hydrogenation will be prohibited as the M-Cu surface becomes high oxygen affinity. The Rh dopant possesses an optimal oxygen affinity, balancing the activation energy barriers of C–O bond scission and *O protonation, potentially leading to the highest selectivity toward C₂H₄ among M-Cu catalysts. The strongest oxophilic property of the Ru-Cu benefits C–O bond cleavage but simultaneously raises the kinetic barrier of *O reduction, which possibly causes a lower selectivity toward C₂H₄ on the Ru-Cu than Rh-/Ir-Cu.

Synthesis and characterization of M-Cu catalysts. Guided by DFT computations, we sought to synthesize a series of M-Cu catalysts by the cation exchange method. For example, Rh-doped CuO pre-catalyst (Rh-CuO) was first prepared by exchanging Cu²⁺ with Rh³⁺ on the Cu(OH)₂ matrix²⁹ followed by calcination treatment (see Methods; Supplementary Fig. 6). The Rh-CuO is in situ reduced to Rh-Cu catalyst at –0.35 V (vs. RHE, thereafter) in a flow cell. In situ Raman spectra show that CuO is electrochemically reduced to metallic Cu as evidenced by the vanishing of characteristic Raman bands associated to copper oxide with reduction time (Fig. 2a). Ex situ X-ray diffraction (XRD) characterization confirms the bulk metallic Cu phase in Rh-Cu catalyst (Supplementary Fig. 7). Additionally, no characteristic peaks attributed to Rh species are observed in XRD patterns for Rh-CuO pre-catalyst and Rh-Cu catalyst, indicating a low Rh content and/or the absence of Rh particles. The mass content of Rh for Rh-Cu is 1.47 wt% determined by inductively coupled plasma optical emission spectrometry (ICP-OES; Supplementary Table 2).

High-resolution X-ray photoelectron spectroscopy (XPS) of Cu $2p$ displays that the Cu valence state is reduced from +2 to 0/+1 during the pre-reduction step (Fig. 2b). High-resolution Rh $3d$ XPS spectrum reveals that Rh mainly presents a trivalent state in Rh-CuO pre-catalyst while a metallic state in Rh-Cu catalyst³⁰ (Fig. 2c). Note that a small fraction of Cu⁺ (Supplementary Fig. 8) and Rh³⁺ species are detected on the Rh-Cu surface, arising from the inevitable oxidation during the sample transfer in XPS analysis³¹. The oxide scale is also detected by ex situ Raman spectra (Supplementary Fig. 9). The Rh doping and in situ pre-reduction cause little variations in morphology and size of catalyst particles as shown in the scanning electron microscopy (SEM) characterizations (Supplementary Figs. 10 and 11). Transmission electron microscopy (TEM) images show that Rh-Cu has a particle size of 15-20 nm (Fig. 2d). The atomic structure of Rh-Cu was further examined by high-angle annular dark-field scanning transmission electron microscopy (HAADF-STEM). Isolated Rh sites (bright dots in blue circles) clearly indicate the monoatomic dispersion of Rh and the absence of Rh clusters or nanoparticles (Fig. 2e and Supplementary Fig. 12). The scanning transmission electron microscopy energy-dispersive X-ray spectroscopy (STEM-EDS) mapping confirms the uniform distribution of Rh single sites on the Cu matrix (Fig. 2f).

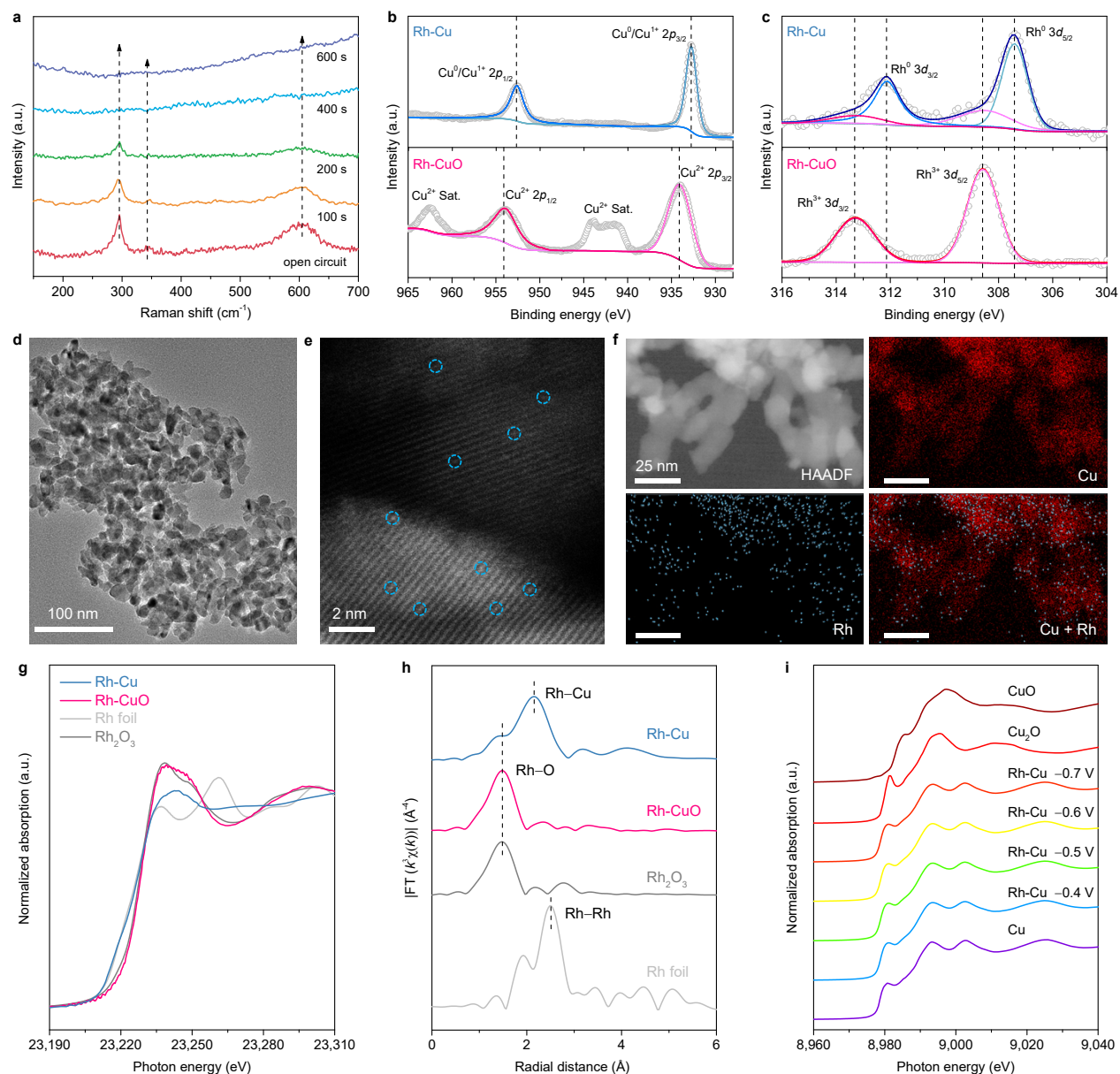


Fig. 2 Structural characterization. **a**, In situ Raman spectrum of the Rh-CuO pre-catalyst at -0.35 V under CO_2RR , the pre-reduction process of Rh-CuO turning into Rh-Cu. **b,c**, Cu $2p$ XPS spectrum (**b**) and Rh $3d$ XPS spectrum (**c**) of the Rh-CuO and Rh-Cu. **d**, TEM image of the Rh-Cu catalyst. **e**, HAADF-STEM image of the Rh-Cu catalyst. The blue circles highlight Rh atoms. **f**, STEM-EDS mapping of the Rh-Cu catalyst, showing atomic dispersion of Rh sites on the Cu matrix. **g,h**, Ex situ XANES spectra (**g**) and EXAFS spectra in R -space (**h**) at the Rh K-edge of the Rh-CuO and Rh-Cu catalyst. The spectra of Rh foil and Rh_2O_3 are shown as references. **i**, In situ Cu K-edge XANES spectra of the Rh-Cu catalyst under CO_2RR . The spectra of Cu, Cu_2O , and CuO are shown as references.

X-ray absorption spectroscopy (XAS) measurements provide information on the electronic states and coordination structures of Rh dopant and Cu matrix. The normalized X-ray absorption near edge structure (XANES) spectra at the Rh K-edge indicate that the chemical states of Rh-CuO pre-catalyst and Rh-Cu catalyst resemble those of Rh₂O₃ and Rh foil, respectively (Fig. 2g). The Rh K-edge extended X-ray absorption fine structure (EXAFS) spectra show that Rh-CuO pre-catalyst has only first shell Rh–O scattering path (Fig. 2h). The Rh-Cu catalyst exhibits one dominated scattering at ~2.15 Å attributed to Rh–Cu bond³² with a shoulder at ~1.51 Å ascribed to Rh–O bond²⁹, mainly arising from the oxidation during ex situ measurements. The absence of Rh–Rh scattering (~2.50 Å)³² corroborates the atomic dispersion of Rh atoms in Rh-Cu, which is also verified by the EXAFS fitting analysis (Supplementary Fig. 13 and Supplementary Table 3). In situ XAS measurements at Cu K-edge support that Cu maintains metallic nature during CO₂RR (Fig. 2i, Supplementary Figs. 14-16). Control samples, including those with different Rh doping contents and other metal dopants (Ir, Ru, Pd, Ag, and Au), were also prepared and characterized similarly (Supplementary Figs. 7, 8, 10, 11, and 17-26).

Electrocatalytic CO₂RR performance of M-Cu catalysts. We evaluated the CO₂RR performances of various M-Cu catalysts in a flow cell with 1 M KOH electrolyte. All M-Cu catalysts showed similar total FE of C₂₊ products (~74 ± 3%) at -0.65 ± 0.01 V (Fig. 3a). Two major CO₂RR products were C₂H₄ and C₂H₅OH accompanied by minor products of acetate (CH₃COO⁻) and *n*-propanol (C₃H₇OH) (Supplementary Fig. 27). However, the distribution of C₂H₄ and C₂H₅OH varied by the dopant. The FE ratio of C₂H₄ to C₂H₅OH (C₂H₄/C₂H₅OH FE ratio) roughly exhibited a volcano-shaped dependence on the surface oxygen affinity of M-Cu. Using the performance of pristine Cu as a benchmark, noble metal dopants such as Rh, Ir, and Ru, with stronger oxygen affinities than Cu, improved the selectivity of C₂H₄ over C₂H₅OH, leading to an enhanced C₂H₄/C₂H₅OH FE ratio. In this oxophilic M-Cu group (M = Rh, Ir, and Ru), the FE of C₂H₄ increased in the order of Cu < Ru-Cu < Ir-Cu < Rh-Cu, while the FE of C₂H₅OH was

in reverse order. The maximum C_2H_4/C_2H_5OH FE ratio was achieved on Rh-Cu, whose value was almost doubled to 4.51 compared to that of 2.33 for pristine Cu. The FE of C_2H_4 and C_2H_4/C_2H_5OH FE ratio dropped with further increasing surface oxygen affinity in the Ru-Cu catalyst. Too strong oxygen binding on Ru site impedes releasing adsorbed *O atoms according to the DFT computations (Fig. 1d). In contrast, Pd, Ag, and Au dopants with weaker oxygen affinity than Cu slightly shifted the selectivity from C_2H_4 to C_2H_5OH , resulting in lower C_2H_4/C_2H_5OH FE ratios than that of pristine Cu. In this oxophobic M-Cu group (M = Pd, Ag, and Au), the selectivity toward C_2H_5OH increased as the oxygen affinity of M-Cu decreased, following the order of Cu < Pd-Cu < Ag-Cu < Au-Cu. The Au-Cu catalyst exhibited the highest C_2H_5OH FE of 24.7% with the lowest C_2H_4/C_2H_5OH FE ratio of 1.75.

The CO_2RR performances at different cathodic potentials followed a similar trend as Fig. 3a (Supplementary Figs. 28-30). As a representative, the catalytic performance of the Rh-Cu at a broad potential window is shown in Fig. 3b-d. The Rh-Cu catalyst exhibited superior C_2H_4 selectivity at the expense of C_2H_5OH formation at potentials more negative than -0.48 V (Fig. 3b), leading to a promoted C_2H_4/C_2H_5OH FE ratio of ~ 4.50 across the potential range of -0.48 to -0.70 V (Fig. 3c). Rh-Cu reached a peak C_2H_4 FE of 61.2% with a partial current density ($j_{C_2H_4}$) of 653 $mA\ cm^{-2}$ at -0.66 V (Fig. 3b, d). As a comparison, pristine Cu yielded C_2H_4 FE of 47.7% and $j_{C_2H_4}$ of 507 $mA\ cm^{-2}$ at the same overpotential. We investigated the possible influence of electrochemical surface area (ECSA), which was determined by the double-layer capacitance method (Supplementary Fig. 31 and Supplementary Table 4). The ECSAs for M-Cu catalysts were nearly invariant, indicating that surface roughness is not the main factor contributing to performance changes. The ECSA-normalized partial current densities of C_2H_4 and C_2H_5OH still followed the same order as geometric ones (Supplementary Fig. 32). The long-term stability of Rh-Cu catalyst was evaluated at -0.66 V, where the best C_2H_4 selectivity was achieved. The Rh-Cu catalyst maintained C_2H_4 FE for at least 35 h operated under a total current density (j_{total}) of

$\sim 1,000 \text{ mA cm}^{-2}$ (Supplementary Fig. 33). Post-reaction characterization showed that the Cu surface retained Rh dopants after the stability test (Supplementary Fig. 34).

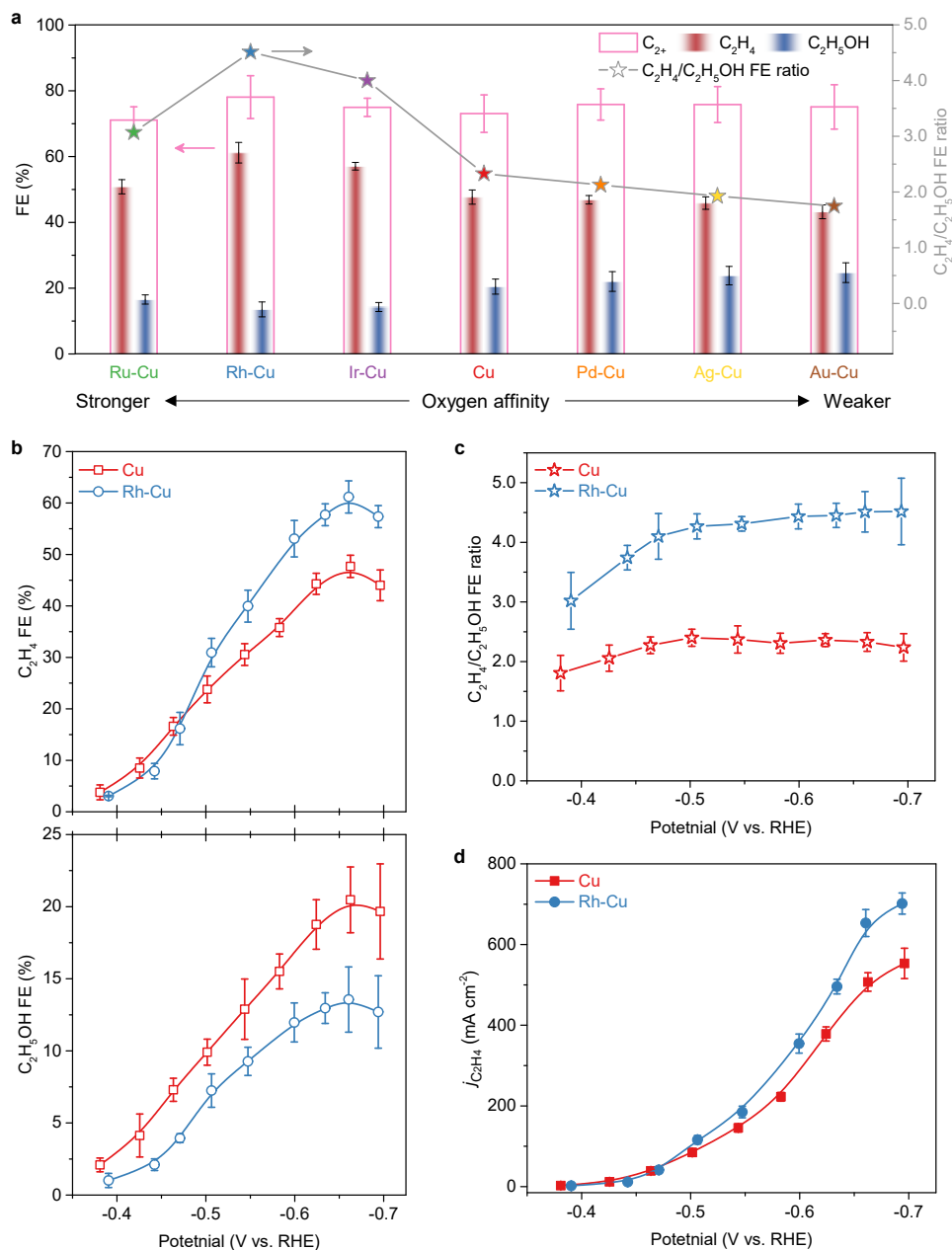


Fig. 3 Electrocatalytic CO₂RR performance. **a**, Comparison of FEs of C₂H₄, C₂H₅OH, and C₂⁺ products, and C₂H₄/C₂H₅OH FE ratios among M-Cu catalysts at $-0.65 \pm 0.01 \text{ V}$. **b-d**, Comparison of FEs of C₂H₄ and C₂H₅OH (**b**), C₂H₄/C₂H₅OH FE ratios (**c**), and $j_{\text{C}_2\text{H}_4}$ (**d**) between the Rh-Cu and pristine Cu catalysts at different potentials. The error bars represent standard deviations from measurements of three independent electrodes.

Validation of Rh doping function. When surface oxygen affinity is enhanced by Rh doping, the improved adsorption of oxygen-bound formyloxyl (*OCHO) intermediate could benefit the formate (HCOO⁻) generation on the Rh-Cu than pristine Cu, especially at low overpotentials^{19,33} (Supplementary Fig. 35). A dramatic enhancement in HCOO⁻ formation over CO was observed if Rh content was further increased (Supplementary Figs. 36 and 37). However, heavy Rh doping reduces C–C coupling rates by limiting *CO coverage because of the even stronger competition from *OCHO intermediate^{33,34}.

In situ Raman measurements were conducted to gain an insight into intermediate adsorption features over the Rh-Cu and pristine Cu using a modified flow cell³⁵. Two pronounced peaks at ~1,462 and ~1,530 cm⁻¹ exclusively emerged on the Rh-Cu catalyst at a low overpotential of -0.45 V (Supplementary Fig. 38). Considering improved yield of HCOO⁻ originated from oxophilic sites at a low overpotential region, we are inclined to assign them to symmetric O–CH–O stretch of bidentate *OCHO and asymmetric O–C–O stretch of carboxylate (*OCO⁻), respectively^{36–38}. These two peaks diminished at -0.65 V, parallel with the selectivity shift from HCOO⁻ to C₂₊ products over the Rh-Cu. Thus, oxophilic sites are likely occupied by intermediates related to C₂ products, such as *CH₂CHO and *O species, at relatively high overpotentials.

However, detecting the C₂-relevant SDI and other intermediates from in situ Raman measurements is extremely challenging due to their high reactivity and low surface coverages^{39,40}. Thus, we sought to perform ethylene oxide reduction reaction (EORR) as a model reaction to simulate the late stages of CO₂RR to C₂H₄ (refs.^{9,23,24}). Prior theoretical and experimental studies suggested that after an epoxy ring opening, ethylene oxide is reduced to C₂H₄ through C–O bond scission, and adsorbed *O atom is released via protonation steps^{9,23,24}, which is analogous to elementary steps of the *CH₂CHO reduction to C₂H₄ (Supplementary Fig. 39a). We observed EORR only produced C₂H₄ without any C₂H₅OH detected on M-Cu catalysts (Supplementary Fig. 40), in agreement with previous experiments^{23,24,41}. The Rh-Cu catalyst showed the lowest onset potential of C₂H₄ formation among all M-Cu (Supplementary Table 5). The reactivity of EORR to

C_2H_4 over M-Cu catalysts followed the same order as the CO_2 -to- C_2H_4 conversion: Rh-Cu > Ir-Cu > Ru-Cu > Cu > Pd-Cu > Ag-Cu > Au-Cu (Supplementary Fig. 39). A volcano correlation of C_2H_4 selectivity vs. surface oxygen affinity also exists for EORR, which supports that tuning surface oxygen affinity could efficiently control the relative stability of the key SDI and $*O$ species at post-C–C coupling stages, and in turn influence the SDS to a specific C_2 product.

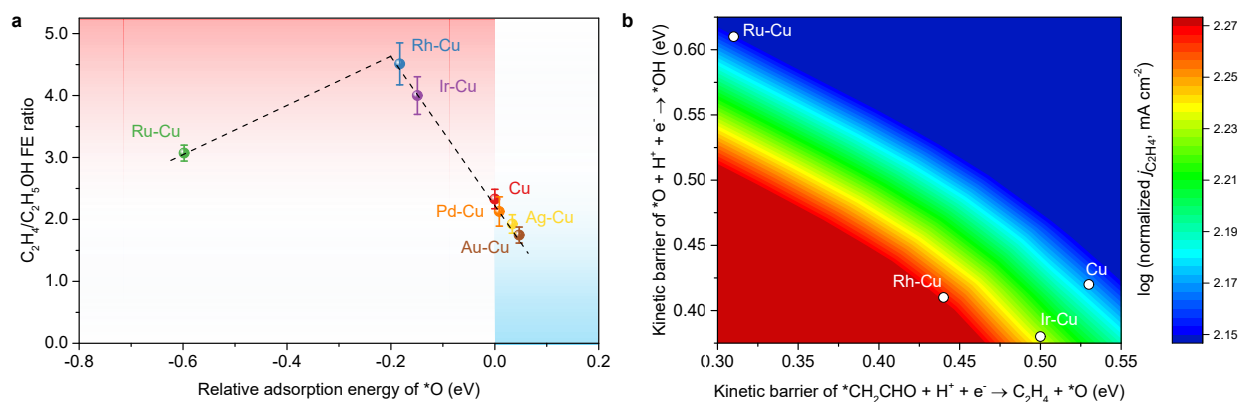


Fig. 4 Correlations between theoretical descriptors and experimental reactivities at -0.65 ± 0.01 V. **a**, Relationship between experimentally measured C_2H_4/C_2H_5OH FE ratio vs. DFT calculated relative adsorption energy of $*O$ intermediate. Dashed line: a volcano relationship for eye guidance. **b**, Two-dimensional plot for ECSA-normalized experimental C_2H_4 activity vs. DFT calculated kinetic barriers of C–O bond scission and subsequent $*O$ protonation along the C_2H_4 pathway.

Correlation between theoretical descriptor and experimental reactivity. Incorporating various oxygen affinity sites, such as noble metal atoms, into the Cu surface can steer the selectivity between C_2H_4 and C_2H_5OH via stabilizing and activating the key SDI in the post-C–C coupling stages. Specifically, introducing stronger oxygen-binding sites (e.g., Rh, Ir, and Ru) to Cu surfaces facilitates C–O bond scission of the SDI (e.g., $*CH_2CHO$), favoring the C_2H_4 formation pathway. An optimal $*O$ adsorption energy is required to reach the maximum selectivity toward C_2H_4 (Fig. 4a), which is derived from balancing the kinetic barriers of C–O bond cleavage in $*CH_2CHO$ and the subsequent hydrogenation of $*O$ adsorbate (Fig. 4b). The Rh-Cu catalyst stands out as the most reactive one for C_2H_4 generation. On the other hand, although Pd-Cu, Ag-Cu, and Au-Cu catalysts

with weaker oxygen affinity induce lower C₂H₄ selectivity and C₂H₄/C₂H₅OH FE ratios than pristine Cu, the extent of decrease is modest. This is consistent with our DFT predictions, where changes in adsorption energies of SDI are marginal because SDIs prefer to adsorb on Cu atoms neighboring oxophobic dopant under the scenario of low doping content (Fig. 1b and Supplementary Fig. 2). However, we infer a superior selectivity of C₂H₅OH over C₂H₄ can be achieved by elevating doping levels, under which intermediates must adsorb directly through oxophobic dopant atoms instead of binding with Cu. For instance, 9-24 at% Ag modified Cu catalysts was reported to reach a comparable or even higher FE of C₂H₅OH than C₂H₄, although a different SDI and mechanism were adopted in that work¹⁷. Nevertheless, surface oxygen affinity might serve as a more universal descriptor to explicate the alteration of selectivity to C₂H₄ vs. C₂H₅OH on various catalysts (Supplementary Note 1).

Collective promotion of RDS and SDS. Benefiting from the high activity and selectivity of C₂H₄, the Rh-Cu catalyst presented a cathodic (half-cell) energy efficiency (EE_{half}) of 37.2% for C₂H₄ in a flow cell at -0.66 V (Supplementary Fig. 41). To further minimize the ohmic resistance and improve the full-cell energy efficiency (EE_{full}), the Rh-Cu catalyst was incorporated into a zero-gap membrane electrode assembly (MEA) electrolyzer (Supplementary Fig. 42). The MEA cell delivered a C₂H₄ FE of 58.2% and $j_{\text{C}_2\text{H}_4}$ of 590 mA cm⁻² at the cell voltage of 3.8 V, where EE_{full} of C₂H₄ was 17.6% (Supplementary Fig. 43). Our previous research demonstrated that segmented tandem electrodes promoted the kinetics of C-C coupling by driving cascade CO₂ → CO → C₂₊ conversion with maximized CO utilization⁴². We intend to promote the activity of both RDS (i.e., C-C coupling step) and SDS (i.e., post-C-C coupling step) by integrating the Rh-Cu and CO-generating ZnO catalysts onto the co-planar segmented tandem electrode (ZnO/Rh-Cu cs-GDE). The ZnO nanoparticles, severing as an extra CO supplier (Supplementary Fig. 44), was placed at the inlet segment of catalyst layer to prolong CO residence time along the length of the electrode (Fig. 5a). In this way, cs-GDE efficiently intensifies *CO surface coverage at the Rh-Cu surface

to enhance the reaction kinetics of the C–C coupling step and in turn maximize the activity and selectivity toward C_{2+} products⁴². The ZnO/Rh-Cu cs-GDE reached C_{2+} FE of 85.4% and C_2H_4 FE of 68.8% at 3.7 V (Fig. 5b), corresponding to a C_2H_4 EE_{full} of 21.4% (Supplementary Fig. 45). The partial current densities of C_2H_4 and C_{2+} products were boosted to 1,012 and 1,256 $mA\ cm^{-2}$, respectively (Fig. 5b).

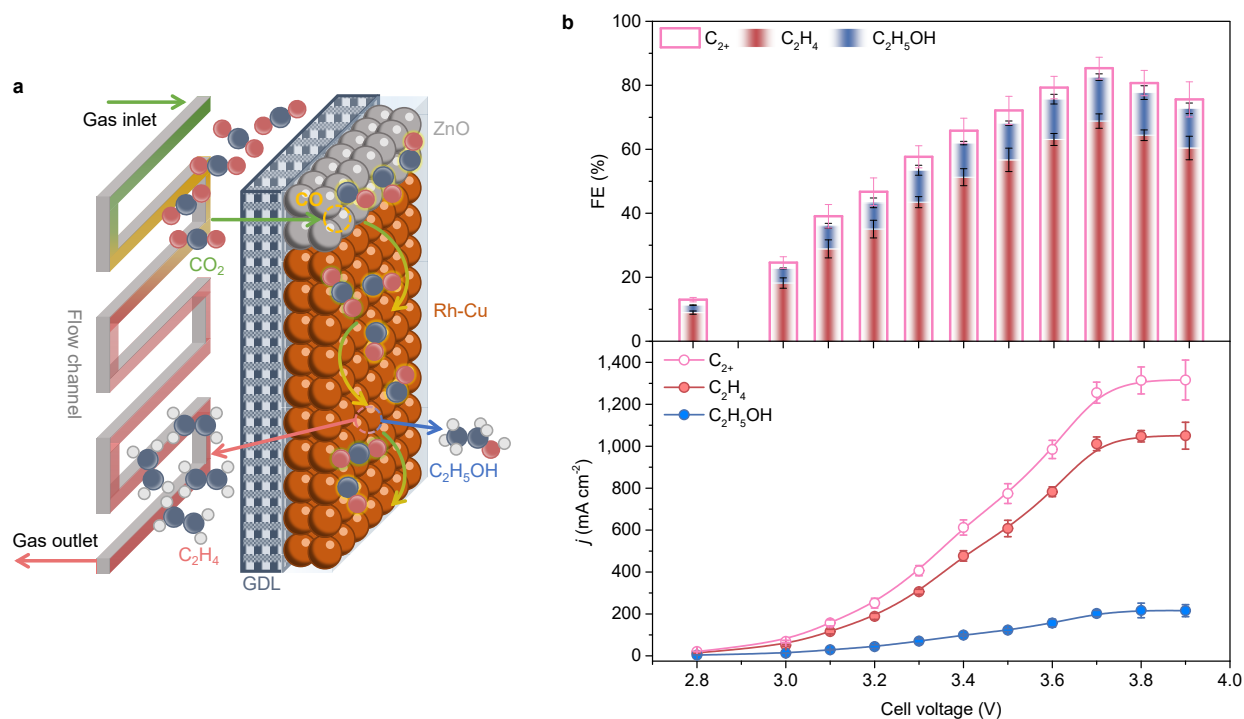


Fig. 5 CO₂RR performance of the ZnO/Rh-Cu cs-GDE in an MEA cell. **a**, Schematic illustration of the tandem electrode structure. **b**, FEs and partial current densities of C_2H_4 , C_2H_5OH , and C_{2+} products at different applied cell voltages.

Conclusions

With synergetic theoretical and experimental results, we demonstrated that single-site doping is an efficient strategy to modulate the Cu surface oxygen affinity, and validate that the oxygen binding energy of the catalyst surface is a generalized descriptor gauging the post-C–C coupling pathway toward formation of C_2H_4 vs. C_2H_5OH . The oxygen affinity of the dopant site on Cu surface has a decisive influence on the C–O bond strength in the SDI as evidenced by the volcano relationship

between C_2H_4 -to- C_2H_5OH FE ratio and relative adsorption energy of $*O$ species. Stronger oxygen-binding sites, such as Rh dopants, favor C_2H_4 formation by facilitating C–O bond scission. On the contrary, weaker oxygen affinity dopants, such as Au, prefer C_2H_5OH generation by preserving C–O bond. Engineering oxygen affinity can be extended to boost other value-added C_1 liquid fuels from CO_2RR , including formate and methanol.

Methods

Computational methods. All calculations were performed with Vienna ab initio simulation package (VASP 5.4.4)⁴³. The exchange-correlation energy was evaluated by the Perdew-Burke-Ernzerhof (PBE) functional⁴⁴ with frozen core electrons treated with projector-augmented-wave (PBE) theory⁴⁵. Valence electrons are taken as: Cu(3d¹⁰4s¹), Ag(4d¹⁰5s¹), Au(5d¹⁰6s¹), Pd(4d⁹5s¹), Ir(5d⁸6s¹), Rh(4d⁸5s¹), Ru(4d⁷5s¹), C(2s²2p²), and O(2s²2p⁴). First order of Methfessel-Paxton smearing was applied with 0.2 eV width⁴⁶. The plane-wave basis was truncated as 450 eV. Brilluoin zones were treated by a Monkhorst-Pack k-points mesh⁴⁷ with 8×8×8 for bulk Cu and 2×2×1 for slab models. A four-layer model of Cu(100) with 2×2 unit cell was built for both pristine or doped surface structure. The bottom two layers were frozen to mimic the bulk structure. Dipole correction was applied for all slab models. The van der Waals interaction correction was applied with the DFT-D3 method⁴⁸. The transition states are found with Climbing image Nudged Elastic Band methods (cNEB)^{49,50}. A water molecule is used as proton shuttle in O–H bond formation reaction steps. The potential-dependent reaction free energies are calculated with the formulas described by Asthagiri and coworkers⁵¹. The Gibbs free energies are calculated as:

$$\Delta G = E_{DFT} + ZPVE + \int_0^T C_p dT - TS$$

where the contributions to the free energy are respectively the total energy of the system by DFT optimization, the zero-point energy, the enthalpic temperature correction, and the entropy correction.

Chemicals and materials. Copper (II) nitrate trihydrate (Cu(NO₃)₂·3H₂O), rhodium(III) chloride (RhCl₃), iridium(III) chloride (IrCl₃), ruthenium (III) chloride trihydrate (RuCl₃·3H₂O), palladium(II) chloride (PdCl₂), silver nitrate (AgNO₃), gold(III) chloride trihydrate (HAuCl₄·3H₂O), sodium hydroxide (NaOH), potassium hydroxide (KOH), phosphate buffer saline (PBS), and gaseous ethylene oxide (≥ 99.5%) were purchased from Sigma Aldrich and used as received.

Catalyst synthesis. Cu(OH)₂ precursor was first synthesized by a precipitation method: 0.5 M Cu(NO₃)₂·3H₂O and 0.5 M NaOH were added dropwise into the deionized water under rapid stirring. The pH of the precipitating solution was kept at ~9. After aging for 8 h with stirring at room temperature and N₂ protection, the blue slurry was washed and centrifuged with water until the pH was close to 7. The precipitates were dried overnight in vacuum to obtain Cu(OH)₂ matrix. For a typical synthesis of the Rh-Cu catalyst, a calculated amount of RhCl₃ solution (1 mg ml⁻¹) was injected into Cu(OH)₂ solution (10 mg ml⁻¹) by a syringe pump at a rate of 10 μl s⁻¹. The mixture solution was stirred vigorously for 5 h. After the cation exchange process, the sample was washed, dried, and annealed at 330 °C for 3 h to obtain Rh-Cu product. Rh-Cu

catalyst was then formed in situ by reducing Rh-CuO precursor on GDE at -0.35 V for 10 min in a flow cell system supplied with CO_2 gas and 1 M KOH as electrolyte. ICP-OES was used to determine the mass loading of Rh. The preparation of other M-Cu samples with similar M atomic contents (Supplementary Table 6) was identical to that of Rh-Cu expect for the use of corresponding metal salts instead of RhCl_3 . The pristine Cu was obtained by direct calcination of $\text{Cu}(\text{OH})_2$ and in sequent electroreduction.

Material characterizations. High-resolution SEM was performed on the FEI Apreo SEM. TEM, HAADF-STEM and EDS elemental mapping were conducted using the JEOL ARM 200F microscope, which is equipped with a cold field emission gun and operated at 200 kV voltage. XPS data was collected from an ESCALAB Xi⁺ spectrometer equipped with a monochromatic Al K α radiation source operating at 200 W. XRD was carried out on the Malvern Panalytical Aeris research edition powder diffractometer using Cu K α radiation. XAS measurements were performed on the Beamline 7-BM and 8-ID of the National Synchrotron Light Source II (NSLS II) at Brookhaven National Laboratory. The Athena and Artemis software in Demeter package were employed for data processing and analysis⁵². The theoretical EXAFS signal was fitted to the experimental EXAFS data in *R*-space by Fourier transforming both the theoretical and experimental data.

Electrochemical measurements. The CO_2 RR performances of all samples were tested in a customized flow cell with 1 M KOH as electrolyte under ambient conditions. To prepare the cathode GDE, the catalyst was dispersed in isopropanol with 5 wt% Nafion to form a homogeneous ink. The catalyst ink was then spray-coated onto the gas diffusion layer (GDL, Sigracet 39BB). The mass loadings of all catalysts were controlled at ~ 0.35 mg cm^{-2} . A Nickel form was used as anode. An anion exchange membrane (FAA-3-PK-130, Fuel Cell Store) was used to separate cathodic and anodic compartments. The electrolyte was fed by syringe pumps (IPS Series, Inovenso) at 2 ml min^{-1} and 5 ml min^{-1} to the cathode and anode chambers, respectively. CO_2 gas was supplied to cathode at 50 sccm via a mass flow controller (Alicat Scientific). A potentiostat (Gamry Interface 1010E) controlled a constant voltage to the flow cell and recorded the corresponding current. A programmable DC power supply (B&K Precision XLN3640) was employed when the current was higher than 1 A. The cathode potential was measured relative to the Ag/AgCl (3 M KCl) reference electrode. All potentials were converted to the RHE scale using: $E_{\text{RHE}} = E_{\text{Ag/AgCl}} + 0.209 \text{ V} + 0.0591 \times \text{pH}$. An *iR* compensation was determined by potentiostatic electrochemical impedance spectroscopy (EIS).

During the electrochemical reaction, an on-line gas chromatograph (GC, SRI Instruments MultipleGas#5) equipped with both a thermal conductivity detector (TCD) and a flame ionization detector (FID) was used to monitor the gas products. To calibrate the outlet gas flow rate of CO_2 , Ar, as an internal standard, was fed at 10 sccm and mixed with the outlet gas stream from the cathode before sampling to the GC loop. The FEs for gas products were calculated

using the following equation:

$$FE(\%) = \frac{zFxV}{j_{total}} \times 100\%$$

where z is the number of electrons transferred for producing a target product; F is the Faraday constant; x is the molar fraction of a target product determined by GC; V is the molar flow rate of gas; j_{total} is the total current density.

Meanwhile, the liquid products after electrolysis were collected and quantified via ^1H NMR (Bruker NEO 400 MHz spectrometer). 500 μl of the electrolyte was mixed with a 100 μl internal standard of 5 mM 3-(trimethylsilyl)propionic-2,2,3,3- d_4 acid sodium salt in D_2O . The standard deviations were calculated based on the measurements of three independent electrodes.

The half-cell and full-cell energy efficiencies of C_2H_4 were calculated as follow:

$$EE_{half}(\%) = \frac{1.23 - E_{\text{C}_2\text{H}_4}^0}{1.23 - E_{\text{cathode}}} \times FE_{\text{C}_2\text{H}_4}(\%)$$

$$EE_{full}(\%) = \frac{1.23 - E_{\text{C}_2\text{H}_4}^0}{E_{\text{cell}}} \times FE_{\text{C}_2\text{H}_4}(\%)$$

where $E_{\text{C}_2\text{H}_4}^0$ is the equilibrium potential for CO_2RR to C_2H_4 , which is 0.08 V (ref.²); E_{cathode} is the applied cathode potential; E_{cell} is the applied cell voltage; $FE_{\text{C}_2\text{H}_4}$ is the Faradaic efficiency of C_2H_4 .

EORR was carried out in a flow cell with 1 M PBS as electrolyte. A neutral pH was chosen to avoid the hydrolysis and polarization of ethylene oxide under acidic and basic conditions⁵³. A Nafion membrane was placed between M-Cu GDE cathode and an IrO_2 GDE anode. The catholyte was degassed by Ar and then bubbled with ethylene oxide to reach 20 mM. During EORR, 2 vol% ethylene oxide balanced by Ar constantly flowed through the cathode. The rest electrochemical measurements and product quantification were identical to those of CO_2RR .

The MEA electrolyzer-based CO_2RR procedure was schematized in Supplementary Fig. 42. The GDE cathode and an IrO_2/Ti mesh anode were separated by a Sustainion anion-exchange membrane (Dioxide Materials). Humidified CO_2 with a rate of 50 sccm was supplied to the cathode. 0.5 M KOH was pumped into anode chamber at 15 ml min^{-1} . A potentiostat (Gamry Interface 5000E) was applied to monitor current densities in a two-electrode system at different cell voltages without iR correction. A cold trap was placed behind the effluent gas at cathode to separate gas products and liquid products. Due to the liquid product crossover, the FEs of liquid products were calculated based on the total amount of the products collected in anode and cathode sides during the same period. The rest procedures were identical to those in a flow cell.

To fabricate the ZnO/Rh-Cu cs-GDE, the uniform Rh-Cu (0.35 mg) segment ($1.8 \text{ (L)} \times 0.5 \text{ (W)} \text{ cm}^2$) was first coated onto the GDL, followed by a condensed ZnO ($\sim 0.04 \text{ mg}$) segment ($0.2 \text{ (L)} \times 0.5 \text{ (W)} \text{ cm}^2$) at the inlet. The area and position of each segment were precisely controlled by a machined template⁴².

In situ Raman spectroscopy measurements. In situ Raman experiment was carried out using a

modified flow cell developed by our group³⁵. The Raman spectrum was recorded on a Renishaw inVia Raman microscope with a 785 nm laser. For each in situ Raman measurement, the acquisition time was 10 s, and the accumulation of scans was 5. Cathode potentials were applied in the potentiostatic mode and converted to the RHE scale accordingly.

References

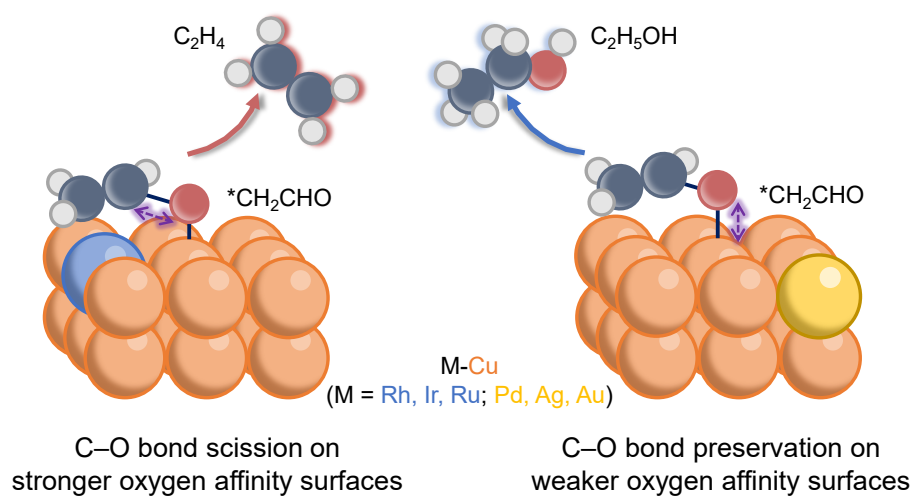
1. Stephens, I. E. L. *et al.* 2022 roadmap on low temperature electrochemical CO₂ reduction. *J. Phys. Energy* **4**, 042003 (2022).
2. Nitopi, S. *et al.* Progress and Perspectives of Electrochemical CO₂ Reduction on Copper in Aqueous Electrolyte. *Chem. Rev.* **119**, 7610–7672 (2019).
3. Xiang, K. *et al.* Boosting CO₂ electroreduction towards C₂₊ products via CO* intermediate manipulation on copper-based catalysts. *Environ. Sci.: Nano* **9**, 911–953 (2022).
4. Murata, A. & Hori, Y. Product Selectivity Affected by Cationic Species in Electrochemical Reduction of CO₂ and CO at a Cu Electrode. *Bull. Chem. Soc. Jpn.* **64**, 123–127 (1991).
5. Lu, X., Shinagawa, T. & Takanabe, K. Product Distribution Control Guided by a Microkinetic Analysis for CO Reduction at High-Flux Electrocatalysis Using Gas-Diffusion Cu Electrodes. *ACS Catal.* **13**, 1791–1803 (2023).
6. Xiao, H., Cheng, T. & Goddard, W. A. Atomistic Mechanisms Underlying Selectivities in C₁ and C₂ Products from Electrochemical Reduction of CO on Cu(111). *J. Am. Chem. Soc.* **139**, 130–136 (2017).
7. Cheng, T., Xiao, H. & Goddard, W. A. Full atomistic reaction mechanism with kinetics for CO reduction on Cu(100) from ab initio molecular dynamics free-energy calculations at 298 K. *Proc. Natl. Acad. Sci. U. S. A.* **114**, 1795–1800 (2017).
8. Luo, W., Nie, X., Janik, M. J. & Asthagiri, A. Facet Dependence of CO₂ Reduction Paths on Cu Electrodes. *ACS Catal.* **6**, 219–229 (2016).
9. Calle-Vallejo, F. & Koper, M. T. M. Theoretical Considerations on the Electroreduction of CO to C₂ Species on Cu(100) Electrodes. *Angew. Chem., Int. Ed.* **52**, 7282–7285 (2013).
10. Cheng, D. *et al.* The nature of active sites for carbon dioxide electroreduction over oxide-derived copper catalysts. *Nat. Commun.* **12**, 395 (2021).
11. Shen, S. *et al.* AuCu Alloy Nanoparticle Embedded Cu Submicrocone Arrays for Selective Conversion of CO₂ to Ethanol. *Small* **15**, 1902229 (2019).
12. Li, J. *et al.* Constraining CO coverage on copper promotes high-efficiency ethylene electroproduction. *Nat Catal* **2**, 1124–1131 (2019).
13. Zhuang, T.-T. *et al.* Steering post-C–C coupling selectivity enables high efficiency electroreduction of carbon dioxide to multi-carbon alcohols. *Nat. Catal.* **1**, 421–428 (2018).
14. Gu, Z. *et al.* Efficient Electrocatalytic CO₂ Reduction to C₂₊ Alcohols at Defect-Site-Rich Cu Surface. *Joule* **5**, 429–440 (2021).
15. Wang, X. *et al.* Efficient electrically powered CO₂-to-ethanol via suppression of deoxygenation. *Nat. Energy* **5**, 478–486 (2020).
16. Li, J. *et al.* Enhanced multi-carbon alcohol electroproduction from CO via modulated hydrogen adsorption. *Nat. Commun.* **11**, 3685 (2020).
17. Li, Y. C. *et al.* Binding Site Diversity Promotes CO₂ Electroreduction to Ethanol. *J. Am. Chem. Soc.* **141**, 8584–8591 (2019).
18. Kuhl, K. P. *et al.* Electrocatalytic Conversion of Carbon Dioxide to Methane and Methanol

- on Transition Metal Surfaces. *J. Am. Chem. Soc.* **136**, 14107–14113 (2014).
19. Feaster, J. T. *et al.* Understanding Selectivity for the Electrochemical Reduction of Carbon Dioxide to Formic Acid and Carbon Monoxide on Metal Electrodes. *ACS Catal.* **7**, 4822–4827 (2017).
 20. Katayama, Y. *et al.* An In Situ Surface-Enhanced Infrared Absorption Spectroscopy Study of Electrochemical CO₂ Reduction: Selectivity Dependence on Surface C-Bound and O-Bound Reaction Intermediates. *J. Phys. Chem. C* **123**, 5951–5963 (2019).
 21. Zhi, X., Jiao, Y., Zheng, Y., Davey, K. & Qiao, S.-Z. Directing the selectivity of CO₂ electroreduction to target C₂ products via non-metal doping on Cu surfaces. *J. Mater. Chem. A* **9**, 6345–6351 (2021).
 22. Zhi, X., Vasileff, A., Zheng, Y., Jiao, Y. & Qiao, S.-Z. Role of oxygen-bound reaction intermediates in selective electrochemical CO₂ reduction. *Energy Environ. Sci.* **14**, 3912–3930 (2021).
 23. Piqué, O., Low, Q. H., Handoko, A. D., Calle-Vallejo, F. & Yeo, B. S. Selectivity Map for the Late Stages of CO and CO₂ Reduction to C₂ Species on Cu Electrodes. *Angew. Chem., Int. Ed.* **60**, 10784–10790 (2021).
 24. Schouten, K. J. P., Pérez Gallent, E. & Koper, M. T. M. Structure Sensitivity of the Electrochemical Reduction of Carbon Monoxide on Copper Single Crystals. *ACS Catal.* **3**, 1292–1295 (2013).
 25. Piqué, O., Viñes, F., Illas, F. & Calle-Vallejo, F. Elucidating the Structure of Ethanol-Producing Active Sites at Oxide-Derived Cu Electrocatalysts. *ACS Catal.* **10**, 10488–10494 (2020).
 26. Seh, Z. W. *et al.* Combining theory and experiment in electrocatalysis: Insights into materials design. *Science* **355**, eaad4998 (2017).
 27. Wu, F. *et al.* Modulating the oxophilic properties of inorganic nanomaterials for electrocatalysis of small carbonaceous molecules. *Nano Today* **29**, 100802 (2019).
 28. Wang, Y.-R. *et al.* Reduction-Controlled Atomic Migration for Single Atom Alloy Library. *Nano Lett.* **22**, 4232–4239 (2022).
 29. Xu, H. *et al.* Cation Exchange Strategy to Single-Atom Noble-Metal Doped CuO Nanowire Arrays with Ultralow Overpotential for H₂O Splitting. *Nano Lett.* **20**, 5482–5489 (2020).
 30. Kibis, L. S., Stadnichenko, A. I., Koscheev, S. V., Zaikovskii, V. I. & Boronin, A. I. XPS Study of Nanostructured Rhodium Oxide Film Comprising Rh⁴⁺ Species. *J. Phys. Chem. C* **120**, 19142–19150 (2016).
 31. Lum, Y. & Ager, J. W. Stability of Residual Oxides in Oxide-Derived Copper Catalysts for Electrochemical CO₂ Reduction Investigated with ¹⁸O Labeling. *Angew. Chem., Int. Ed.* **57**, 551–554 (2018).
 32. Liu, H. *et al.* Efficient Electrochemical Nitrate Reduction to Ammonia with Copper-Supported Rhodium Cluster and Single-Atom Catalysts. *Angew. Chem., Int. Ed.* **61**, e202202556 (2022).

33. Su, D.-J. *et al.* Kinetic Understanding of Catalytic Selectivity and Product Distribution of Electrochemical Carbon Dioxide Reduction Reaction. *JACS Au* **3**, 905–918 (2023).
34. Huang, Y., Handoko, A. D., Hirunsit, P. & Yeo, B. S. Electrochemical Reduction of CO₂ Using Copper Single-Crystal Surfaces: Effects of CO* Coverage on the Selective Formation of Ethylene. *ACS Catal.* **7**, 1749–1756 (2017).
35. Li, Z. *et al.* Planar defect-driven electrocatalysis of CO₂-to-C₂H₄ conversion. *J. Mater. Chem. A* **9**, 19932–19939 (2021).
36. Bohra, D. *et al.* Lateral Adsorbate Interactions Inhibit HCOO⁻ while Promoting CO Selectivity for CO₂ Electrocatalysis on Silver. *Angew. Chem., Int. Ed.* **58**, 1345–1349 (2019).
37. Firet, N. J. & Smith, W. A. Probing the Reaction Mechanism of CO₂ Electroreduction over Ag Films via Operando Infrared Spectroscopy. *ACS Catal.* **7**, 606–612 (2017).
38. Shan, W. *et al.* In Situ Surface-Enhanced Raman Spectroscopic Evidence on the Origin of Selectivity in CO₂ Electrocatalytic Reduction. *ACS Nano* **14**, 11363–11372 (2020).
39. Goodpaster, J. D., Bell, A. T. & Head-Gordon, M. Identification of Possible Pathways for C–C Bond Formation during Electrochemical Reduction of CO₂: New Theoretical Insights from an Improved Electrochemical Model. *J. Phys. Chem. Lett.* **7**, 1471–1477 (2016).
40. Birdja, Y. Y. *et al.* Advances and challenges in understanding the electrocatalytic conversion of carbon dioxide to fuels. *Nat. Energy* **4**, 732–745 (2019).
41. Schouten, K. J. P., Kwon, Y., Ham, C. J. M. van der, Qin, Z. & Koper, M. T. M. A new mechanism for the selectivity to C₁ and C₂ species in the electrochemical reduction of carbon dioxide on copper electrodes. *Chem. Sci.* **2**, 1902–1909 (2011).
42. Zhang, T. *et al.* Highly selective and productive reduction of carbon dioxide to multicarbon products via in situ CO management using segmented tandem electrodes. *Nat. Catal.* **5**, 202–211 (2022).
43. Kresse, G. & Furthmüller, J. Efficiency of ab-initio total energy calculations for metals and semiconductors using a plane-wave basis set. *Computat. Mater. Sci.* **6**, 15–50 (1996).
44. Perdew, J. P., Burke, K. & Ernzerhof, M. Generalized Gradient Approximation Made Simple. *Phys. Rev. Lett.* **77**, 3865–3868 (1996).
45. Blöchl, P. E. Projector augmented-wave method. *Phys. Rev. B* **50**, 17953–17979 (1994).
46. Methfessel, M. & Paxton, A. T. High-precision sampling for Brillouin-zone integration in metals. *Phys. Rev. B* **40**, 3616–3621 (1989).
47. Monkhorst, H. J. & Pack, J. D. Special points for Brillouin-zone integrations. *Phys. Rev. B* **13**, 5188–5192 (1976).
48. Grimme, S., Antony, J., Ehrlich, S. & Krieg, H. A consistent and accurate ab initio parametrization of density functional dispersion correction (DFT-D) for the 94 elements H-Pu. *J. Chem. Phys.* **132**, 154104 (2010).
49. Henkelman, G., Uberuaga, B. P. & Jónsson, H. A climbing image nudged elastic band method for finding saddle points and minimum energy paths. *J. Chem. Phys.* **113**, 9901–9904 (2000).

50. Henkelman, G. & Jónsson, H. Improved tangent estimate in the nudged elastic band method for finding minimum energy paths and saddle points. *J. Chem. Phys.* **113**, 9978–9985 (2000).
51. Nie, X., Luo, W., Janik, M. J. & Asthagiri, A. Reaction mechanisms of CO₂ electrochemical reduction on Cu(111) determined with density functional theory. *J. Catal.* **312**, 108–122 (2014).
52. Ravel, B. & Newville, M. ATHENA, ARTEMIS, HEPHAESTUS: data analysis for X-ray absorption spectroscopy using IFEFFIT. *J. Synchrotron Radiat.* **12**, 537–541 (2005).
53. Melhem, G. A. *et al.* Kinetics of the reactions of ethylene oxide with water and ethylene glycols. *Process Saf. Prog.* **20**, 231–246 (2001).

TOC



Data availability

All the data that support the findings of this study are available in the main text and the Supplementary Information file, or from the corresponding author on reasonable request.

Acknowledgements

xxx. P.W. and T.P.S. acknowledge the funding support from xxx. S.Y. acknowledges the use of facilities within the Eyring Materials Center at Arizona State University, supported in part by NNCI-ECCS-1542160. V.K.R.K., Y.F. and V.S. acknowledge the funding from the UC CEAS Pilot Program NOEMA. Z.L. acknowledges URC Graduate Student Stipend awarded by the Office of Research at University of Cincinnati. Z.L. thanks Dr. Xiao Shang for discussing catalyt synthesis and reaction mechanisms.

Author contributions

Z.L. and P.W. conceptualized the project under the supervision of T.P.S. and J.W. Z.L. synthesized catalysts, performed the electrochemical tests, and analyzed experimental data with the help of T.I. and T.Z. P.W. performed DFT simulation. S.Y., X.L. and Z.L. conducted the catalyst characterization with the help of Y.B, J.L. and A.S. Z.L. and V.K.R.K. carried out in situ Raman measurements with the assistance of Y.F. and V.S. S.X., J.D.J., L.M., A.I.F. and S.D.S carried out XAS measurements and analyses. Z.L., P.W., J.R., S.Y., T.P.S. and J.W. wrote the manuscript. All authors discussed the results and commented on the manuscript.

Competing interests

The authors declare no competing interests.